NeuroImage 193 (2019) 10–24

Contents lists available at ScienceDirect

NeuroImage

journal homepage: www.elsevier.com/locate/neuroimage

MEDUSA: A GPU-based tool to create realistic phantoms of the brain microstructure using tiny spheres

Kévin Ginsburger [a,b,*,1], Felix Matuschke [c,1], Fabrice Poupon [a,b], Jean-François Mangin [a,b], Markus Axer [c], Cyril Poupon [a,b]

[a] CEA DRF/ISVFJ/Neurospin/UNIRS, Gif-sur-Yvette, France
[b] Université Paris-Saclay, Orsay, France
[c] Research Centre Juelich, Institute of Neuroscience and Medicine, Juelich, Germany

ARTICLE INFO

Keywords:
GPU
Phantom generation
White matter
Diffusion MRI

ABSTRACT

A GPU-based tool to generate realistic phantoms of the brain microstructure is presented. Using a spherical meshing technique which decomposes each microstructural item into a set of overlapping spheres, the phantom construction is made very fast while reliably avoiding the collisions between items in the scene. This novel method is applied to the construction of human brain white matter microstructural components, namely axonal fibers, oligodendrocytes and astrocytes. The algorithm reaches high values of packing density and angular dispersion for the axonal fibers, even in the case of multiple white matter fiber populations and enables the construction of complex biomimicking geometries including myelinated axons, beaded axons, and glial cells. The method can be readily adapted to model gray matter microstructure.

1. Introduction

One key objective of non-invasive medical imaging techniques, such as diffusion MRI, is the ability to relate the measured macroscopic signal to the underlying microscopic properties of the observed tissue. Several analytical approaches have been developed in the past, leading to the modeling of tissue cellular environments using simple glyphs, such as cylinders and ellipsoids, which are not representative of actual tissues. The main reason for keeping such over-simplistic geometries is that analytical solutions of the diffusion equation only exist for a limited number of geometries (Neuman, 1974; Vangelderen et al., 1994; Sen and Basser, 2005).

The popularization of high performance computing, either based on the use of GPU or multi-core CPU, pushed the community to go beyond analytical models by considering *in silico* approaches. Simulations offer a unique opportunity to enhance the realism of tissue modeling, using computational frameworks that more robustly capture the mapping between features derived from diffusion-weighted MR signals and ground truth microstructure parameters (Nedjati-Gilani et al., 2017).

To tackle the particularly ill-posed problem of tissue-to-signal relationship, the use of virtual histology seems to be a credible approach: if the geometrical properties of the generated numerical tissues are well known and controlled, the synthesis of the associated signal -using, in the case of diffusion MRI, Monte-Carlo simulations of the diffusion process- for a wide range of different geometries will provide a valuable set of data that could be used to model this relationship, with the help of machine learning techniques. Of course, the new problem posed by virtual histology is to design a generative model creating realistic numerical scenes that represent sufficiently well the biological environment.

In the particular field of brain microstructure, several tools have been proposed to construct numerical phantoms of gray and white matter (Balls and Frank, 2009; Budde and Frank, 2010; Fieremans et al., 2010; Harkins and Does, 2016; Neher et al., 2014; Landman et al., 2010; Lin et al., 2016; Liu et al., 2004; Stanisz et al., 1997; Szafer et al., 1995; Rensonnet et al., 2019; Van Nguyen et al., 2018). The AxonPacking simulator (Mingasson et al., 2017) performs 2-dimensional random disks packing to generate white matter substrates, thus not enabling to model 3-dimensional effects such as local and global angular dispersion of axons, as well as axonal swelling or beading. The CAMINO simulator (Hall and Alexander, 2009) enables the construction of white matter

* Corresponding author. CEA DRF/ISVFJ/Neurospin/UNIRS, Gif-sur-Yvette, France.
E-mail address: kginsburger@gmail.com (K. Ginsburger).
URL: http://cati-neuroimaging.com (J.-F. Mangin).
[1] These authors contributed equally to this work.

https://doi.org/10.1016/j.neuroimage.2019.02.055
Received 8 November 2018; Received in revised form 18 February 2019; Accepted 21 February 2019
Available online 5 March 2019

phantoms including regularly-packed cylinders, crossing cylinders, irregularly-packed cylinders with distributed radii and mesh substrates. The generation of geometries from scratch (i.e. without any histological input) is thus limited to straight cylinders, with at most two fiber populations, which is not sufficient to fully represent the complexity of white matter.

The Diffusion Microscopist Simulator (Yeh et al., 2013) (DMS) has recently been improved and includes, besides all the tools provided by CAMINO, the possibility to model any number of fiber populations, add global angular dispersion, tortuosity and beading to axons as well as myelin and Ranvier nodes (Ginsburger et al., 2018). However, the generative model employed in DMS, which is similar to CAMINO, is mainly based on the representation of axonal fibers as cylinders, which considerably limits the values of angular dispersion and packing densities that can be achieved with this type of algorithm. Moreover, neither CAMINO nor DMS have yet provided a tool to create synthetic glial cells, such as oligodendrocytes and astrocytes, which are prevalent in white matter and might thus have an important impact on the observed diffusion-weighted MRI signal (Marco et al., 2018).

Several frameworks have also been proposed in recent years to create gray matter phantoms (Van Nguyen et al., 2015; Cuntz et al., 2010). What seems to be an extension to CAMINO for gray matter has recently been presented and seems a most promising tool to generate different types of neural cells, using a reduced set of geometrical parameters (Palombo et al., 2018). However, the presented tissue generator does not provide any packing method for the constructed digital cells while preventing overlap between generated cells is one of the main challenge of phantom construction.

In this work, the Microstructure Environment Designer with Unified Sphere Atoms (MEDUSA) is presented, which enables to represent any kind of cellular type (axons, astrocytes and oligodendrocytes, neurons) using a spherical meshing technique. Since all microstructural items are represented as a set of overlapping spheres, the packing of such items can be performed using an algorithm which solves collisions between spheres in a generic way that does not require to consider the particular type of biological structure it is dealing with. Such an algorithm, written in CUDA, enables a very fast resolution of all collisions in each constructed scene. This new method is applied here to construct realistic phantoms of white matter tissues, including all the features already provided by DMS to create axonal fibers, while reaching much higher values of angular dispersion and packing density, and covering the construction of astrocytes and oligodendrocytes to enhance the realism of the phantoms. The putative construction of realistix gray matter phantoms using such an approach is also illustrated.

2. Methods

2.1. The synthesis of various white matter cells

2.1.1. Axonal fibers

Axonal fibers are the principal component of white matter. In a typical imaging voxel, complex configurations of fibers due to the presence of several heterogeneous populations are likely to happen. Several studies in the field of diffusion MRI have reported a percentage of around 60 percent of voxels containing crossing, kissing or splitting fibers at the conventional millimeter resolution of diffusion MRI data (Behrens et al., 2007).

Each fiber population is composed of myelinated or unmyelinated axons, which diameter distribution can be represented by a Gamma function whose shape and scale parameters can vary from one population to another (Assaf et al., 2008; Alexander et al., 2010). Other more realistic axonal diameter distributions can also be used, such as the lognormal or generalized extreme value distributions (Sepehrband et al., 2016).

Myelinated axons are regularly interrupted by Ranvier nodes along the axon main direction (Salzer, 1997); the internode distance d has been extensively studied in (Rushton, 1951) leading to the maximum conduction relationship

$$\frac{d}{D} \propto g \sqrt{\log\left(\frac{1}{g}\right)} \tag{1}$$

where D is the external diameter of the axon (including the myelin sheath), and g is the g-ratio defined as the ratio between the axonal membrane and the external myelin sheath outer membrane diameters.

The fibers of a given population depict a macroscopic angular dispersion that corresponds to the global misalignment of axons, as well as a local tortuosity-which can be defined as the ratio between the geodesic distance along the curvilinear frame defined by the centroid axis of the axonal fiber and the Euclidean distance between the two extremities of the fiber.

It is not clear whether the axon diameter and myelin sheath thickness remain constant along the axon; several studies have assumed this absence of variation (Beaulieu, 2002; Daducci et al., 2016) whereas other studies tend to indicate a variation of the axon diameter (Lee et al., 2018; Abdollahzadeh et al., 2017); in particular, it is known that membrane injury can induce axonal beading for instance due to cytoskeletal damage (Budde and Frank, 2010; Tang-Schomer et al., 2012).

Table 1 shows all the geometrical parameters that can be set to construct each population of axonal fibers with a controlled degree of realism using MEDUSA. Fig. 1 illustrates the influence of each parameter.

To construct one fiber in a given population, the algorithm draws the fiber orientation from a Watson distribution (Fisher et al., 1993), whose κ parameter is set according to the desired value of global angular dispersion and the mean value is equal to the mean orientation of the fiber population. Other orientation dispersion distributions can also be used, as shown at the end of the Results section. A starting point is then drawn randomly on the minimal sphere containing the scene field of view, and a straight fiber grows in the direction of the fiber orientation, by successively adding overlapping spheres of constant radius r in this direction. The radius r of the spheres is equal to the axonal radius. The distance d_s between each sphere center is a tradeoff between a representative fiber structure and a treatable amount of spheres. We typically choose $d_s = r/4$. The fiber stops growing when it reaches the other end of the containing sphere. Only the spheres that are inside the field of view are kept. Fibers are created until the volume fraction is reached for a given fiber population.

Once those straight fibers made of spheres have been created, the

Table 1
List of control parameters used to generate populations of axonal fibers in the phantom generation algorithm.

Geometrical characteristics	Control parameter names	Parameters description
Axon diameter distribution	$\mathbf{u}$	Mean orientation of the population
	Φ_f	Target volume fraction of the population
	$\langle D_f \rangle$	Axon diameter mean value
	σ_{D_f}	Axon diameter standard deviation
Global angular dispersion	GAD	Target global angular dispersion
Local tortuosity	LAD	Additional angular dispersion due to tortuosity
Ranvier nodes	$\langle R \rangle$	Mean ratio (internodal length)/(node width)
	σ_R	Ratio standard deviation
Beading	$< BS >$	Beading spacing mean value
	σ_{BS}	Beading spacing standard deviation
	$< BA >$	Beading amplitude mean value
	σ_{BA}	Beading amplitude standard deviation
Myelin sheath	$< g >$	Mean g-ratio value
	σ_g	g-ratio standard deviation

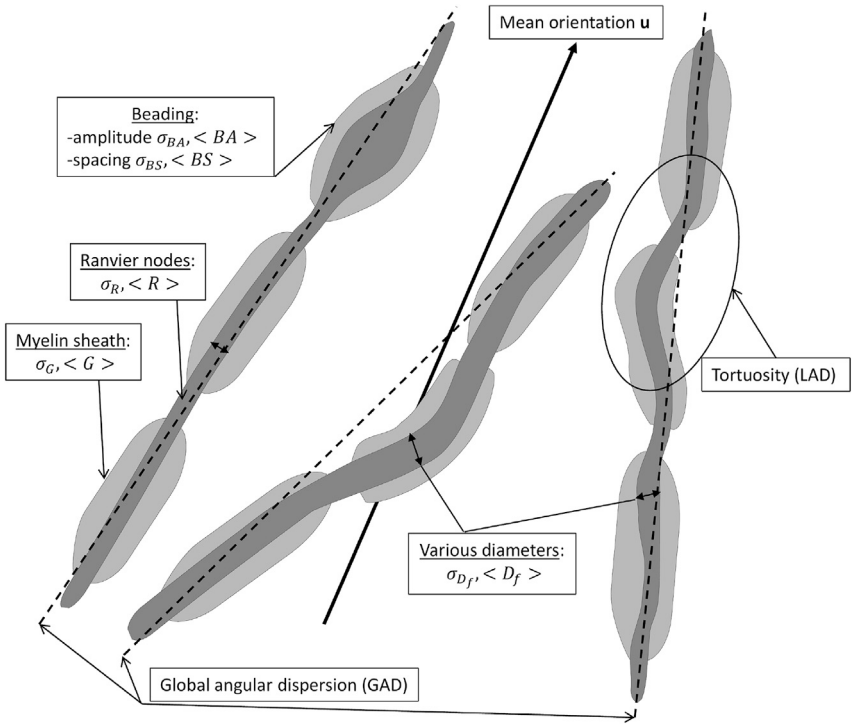

Fig. 1. Illustration of the axon creation procedure. The shown parameters correspond to Table 1.

addition of tortuosity is done in a second step by randomly deforming portions of fibers using Gaussian distribution functions, until the required value of local angular dispersion (also called tortuosity) has been reached, as shown in Fig. 2.

Beading, consisting in local variations of the axon diameter, can also be rendered by applying sinusoidal functions to the radii of spheres on some random portions of the axonal fibers, as illustrated in Fig. 3. This feature can be used to represent swollen fiber regions due to cytoskeletal damage (Budde and Frank, 2010; Tang-Schomer et al., 2012) as well as healthy white matter tissues where beaded regions can also be found, as demonstrated in two recent works (Lee et al., 2018; Abdollahzadeh et al., 2017), suggesting that modeling axons by straight cylinders may not be accurate.

The creation of a myelin sheath and Ranvier nodes is done only after the collision solver algorithm has been applied. Indeed, the axonal fiber spheres which have been created previously correspond to the outer axonal membranes. Once the final position of all outer axonal fiber spheres is known, the creation of the inner axonal membrane is done simply by duplicating all the spheres with a smaller radius, whose value is computed using the value of the *g*-ratio required by the user. The myelin sheath consists of the space between the spheres from the inner and the outer axonal membranes.

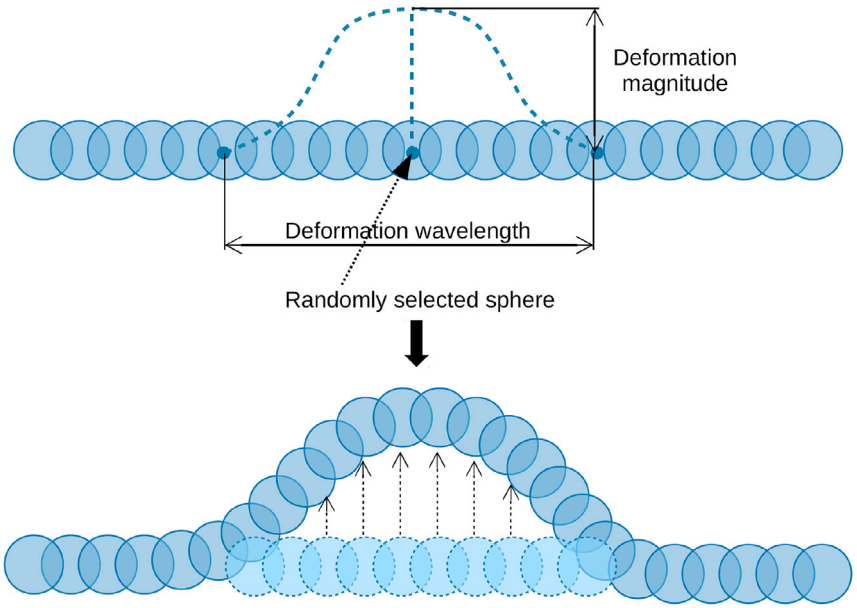

Fig. 2. Illustration of the induction of tortuosity within axonal fibers. A Gaussian deformation is applied at a randomly selected sphere, in a random direction orthogonal to the main fiber orientation.

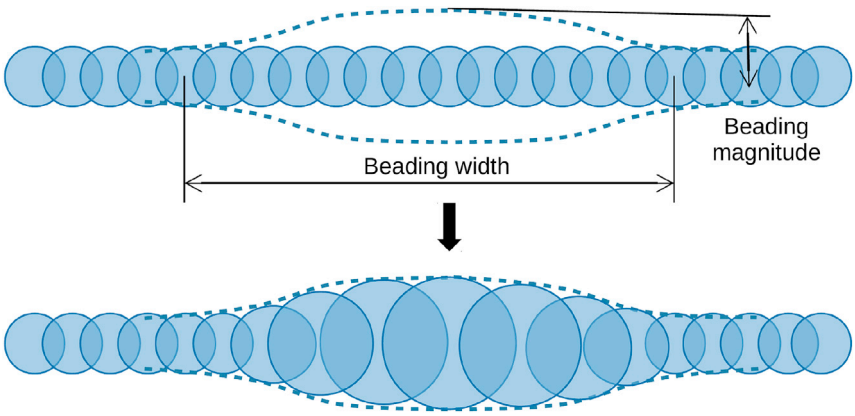

Fig. 3. Illustration of the induction of beading within axonal fibers. Fiber spheres are swollen according to a sinusoidal or bell-shaped function to locally increase axonal diameter.

Ranvier nodes are then added by setting the sphere radius of external membrane spheres to the value of the corresponding inner membrane sphere, at regular intervals whose value correspond to the internodal length, computed using the maximal conduction relationship (Rushton, 1951). The creation process is explained in Fig. 4.

2.1.2. Astrocytes

Astrocytes are the most numerous and diverse glial cells in the central nervous system, and they have been attributed a role in the development of neurons e.g. formation and pruning of synapses, as well as in the development or repair of acute CNS trauma or chronic neurodegenerative diseases (Lundgaard et al., 2014). We only focus here on fibrous astrocytes, the type of astrocytes populating white matter tissues. Experimental evidence points to fibrous astrocytes as being crucial in facilitating normal myelination during development, maintaining the right environment for oligodendrocytes and also ion buffering and metabolic supply throughout adulthood (Lundgaard et al., 2014; Oberheim et al., 2009).

According to (Oberheim et al., 2009), the processes of fibrous astrocytes are long -up to 300μm- and their density is $\sim$ 200 000 cells per mm^3. Their processes are radially oriented in the direction of the axon bundles, relatively unbranched, and extend evenly from a small cell body. The cell bodies are equally spaced, probably due to the fact that they provide a structural support for the axons tract (Oberheim et al., 2009).

As shown in Table 2, the construction of astrocytes requires the definition of several geometrical parameters per astrocyte population, such as the diameter of the astrocyte body and processes, the total diameter of the astrocyte, the volume fraction, and the balancing factor which will be defined immediately afterwards.

The generative model used to construct astrocytes is inspired from the method presented in (Cuntz et al., 2010; Palombo et al., 2018) for the construction of neural cells. As illustrated in Fig. 5, the basic idea relies on the construction of a minimum spanning tree (MST) from a set of points in 3D. The distance cost function used to compute the MST is composed of two components, weighted by a balancing factor b_f: the wiring cost, corresponding to the Euclidean distance between nodes of

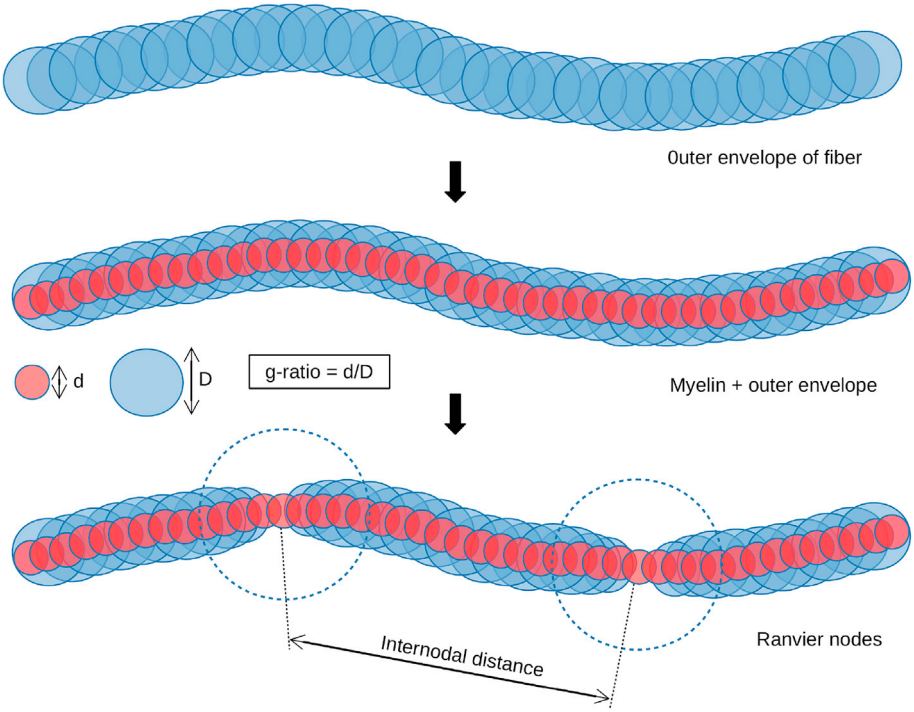

Fig. 4. Illustration of the creation of a myelin sheath and Ranvier nodes on axonal fibers. The spheres from inner axonal membrane (in red) are created after the collision solver. Their diameter is computed using the *g*-ratio and the outer axonal diameter.

Table 2
List of control parameters used to generate populations of astrocytes in the phantom generation algorithm.

Geometrical characteristics	Control parameters names	Parameters description
Astrocyte distribution	Φ_a	Volume fraction
	$\langle D_{at} \rangle$	Total diameter mean
	$\sigma_{D_{at}}$	Total diameter standard deviation
Astrocyte body	$< D_{ab} >$	Body diameter mean
	$\sigma_{D_{ab}}$	Body diameter standard deviation
Astrocyte processes	$< D_{ap} >$	Processes diameter mean
	$\sigma_{D_{ap}}$	Processes diameter standard deviation
	BF_a	Balancing factor
	AT_a	Angular threshold

the tree, and the conduction cost, corresponding to the path length from the astrocyte body to each given node. A balancing factor $b_f = 1$ leads to a completely stellate structure, and a progressive diminution of b_f leads to the apparition of branching processes whose number can therefore be controlled.

The 3D point cloud from which the MST is computed is made of random points drawn inside a sphere whose radius is equal to the total radius of the astrocyte. However, in order to satisfy the constraint that astrocyte processes are radially oriented in the direction of axon bundles, 3D points whose position differ from the main axon bundles directions with a certain angular threshold (typically 30) are discarded. The astrocyte soma is located at the root node of the MST.

Tortuosity is also added to the astrocyte processes following a similar procedure as for axons, i.e. randomly applying Gaussian deformation in a random direction on each branch of the processes. Finally, in order to improve the realism of the constructed astrocytes, the radii r of processes decrease when the distance d to the soma increases

$$r = r_0 e^{(-\alpha . d/R)} \tag{2}$$

where R is the total radius of the generated astrocyte, and α is a tunable parameter (typically equal to 2). Indeed, microscopic images of astrocytes in (Oberheim et al., 2009) strongly suggest that the diameter of astrocyte processes decreases with the distance to the soma. Similar observations were done for dendrite processes which were modeled with decreasing diameters when the distance to the soma increases in (Cuntz et al., 2010). However, equation (2) is not based on any biological evidence and was employed for rendering purposes only. Further investigations are needed to obtain a more biologically relevant equation to model the decreasing radius of astrocyte processes.

2.1.3. Oligodendrocytes

Oligodendrocytes are glial cells with fewer processes than astrocytes. The main function of oligodendrocytes is the production of myelin which insulates axons in the central nervous system. Oligodendrocytes were first described in (del Río-Hortega, 1928), where these cells were classified into four main phenotypes. We here focus on type II oligodendrocytes, which are very similar to type I oligodendrocytes with a small rounded body producing four to six primary processes, which branch and myelinate 10 to 30 thin (diameter $< 2\mu m$) axons, each secondary process forming a single internodal myelin segment of approximately $100 - 200\mu m$ length. Type II oligodendrocytes are predominant in white matter, where they are the primary cell type.

As shown in Table 3, the construction of oligodendrocytes requires the definition of several geometrical parameters per oligodendrocyte population, such as the diameter of the body and processes, the total diameter of the oligodendrocyte, the volume fraction, and the number of

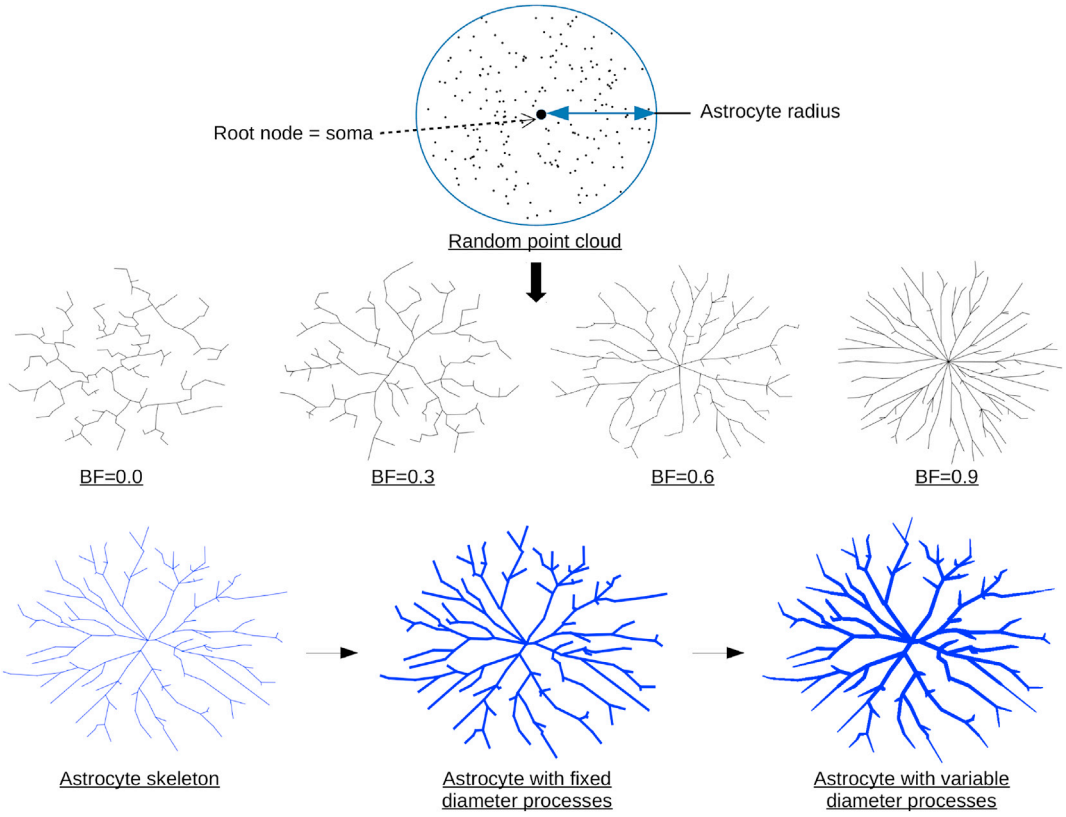

Fig. 5. Illustration of the astrocyte creation procedure. The scheme shows that each astrocyte is created from a random point cloud. Euclidean minimum spanning trees created at different values of the balancing factor are shown, ranging from perfect minimum spanning trees to almost direct connections to the root node. The function used to model processes diameter is also shown here in 2D.

Table 3
List of control parameters used to generate populations of oligodendrocytes in the phantom generation algorithm.

Geometrical characteristics	Control parameter names	Parameters description
Oligodendrocyte distribution	Φ_o	Volume fraction
	$< D_{ot} >$	Total diameter mean
	$\sigma_{D_{ot}}$	Total diameter standard deviation
Oligodendrocyte body	$< D_{ob} >$	Body diameter mean
	$\sigma_{D_{ob}}$	Body diameter standard deviation
Oligodendrocyte processes	$< D_{op} >$	Processes diameter mean
	$\sigma_{D_{op}}$	Processes diameter standard deviation
	S_r	Axons search radius
	P_c	Processes count
	BF_o	Balancing factor

processes. Similar to astrocytes, oligodendrocytes creation also involves the construction of a MST using the exact same method described for astrocytes.

As shown in Fig. 6, the main difference between astrocyte generation and oligodendrocyte generation resides in the fact that oligodendrocytes processes must be attached to the axonal outer membrane, since they are involved in the creation of the myelin sheath. Thus, a search radius also has to be specified for each oligodendrocyte, which defines the area in which the oligodendrocyte myelinate axons. Depending on the number of processes count for each particular oligodendrocyte, a set of spheres from the external membranes of axons present in the area are selected, which constitute connection points for the oligodendrocyte. The algorithm checks that the selected axonal spheres are not located around Ranvier nodes, and axonal spheres are preferentially chosen around the center of the internode region, using a Gaussian distribution. This particular connection feature of oligodendrocytes has required the creation of a look-up-table that identifies all the external axonal spheres present in a given sub-region of the scene field of view.

2.2. A generic approach to generate packings of non-colliding cells using spheres

The main objective of the presented phantom generation approach is to be able to represent a wide variety of cell types present in the human brain while being able to solve the collisions between the generated structures using one simple packing algorithm. To this end, the use of overlapping spheres of varying sizes is particularly suitable for packing, since it only involves the computation of distances between spheres, thus decreasing computational complexity with respect to classical triangular mesh approaches, while maintaining a high representational power.

The idea to represent fibers as chains of spheres, which is here generalized to any kind of cell type, was first considered in (Altendorf and Jeulin, 2011). The essential idea is the force-biased spheres packing algorithm, whose implementation is explained here.

2.2.1. Repulsion forces

Let us consider that, in the first step of the phantom generation framework, a set of microstructural items I has been created, according to a set of geometrical parameters provided by the user. Those items belong to one or several cell populations, such as axonal fibers, astrocytes or oligodendrocytes. Each microstructural item $i \in I$ is made of overlapping spheres and since the collision solver has not yet been used, there exists some overlapping between spheres of different items, which should be removed.

At this point, each sphere in the scene is represented as a simple structure comprising the position of its center, its radius, the ID of the cell population it belongs to, and the ID of the cell item it belongs to (ID means here the identity of the population or item it refers to). This set of spheres is fed into a GPU-based collision solver (written in CUDA), which computes and applies repulsion forces between spheres which do not belong to the same cell item. More precisely, the repulsion force for a pair of overlapping spheres belonging to distinct cell items describes the

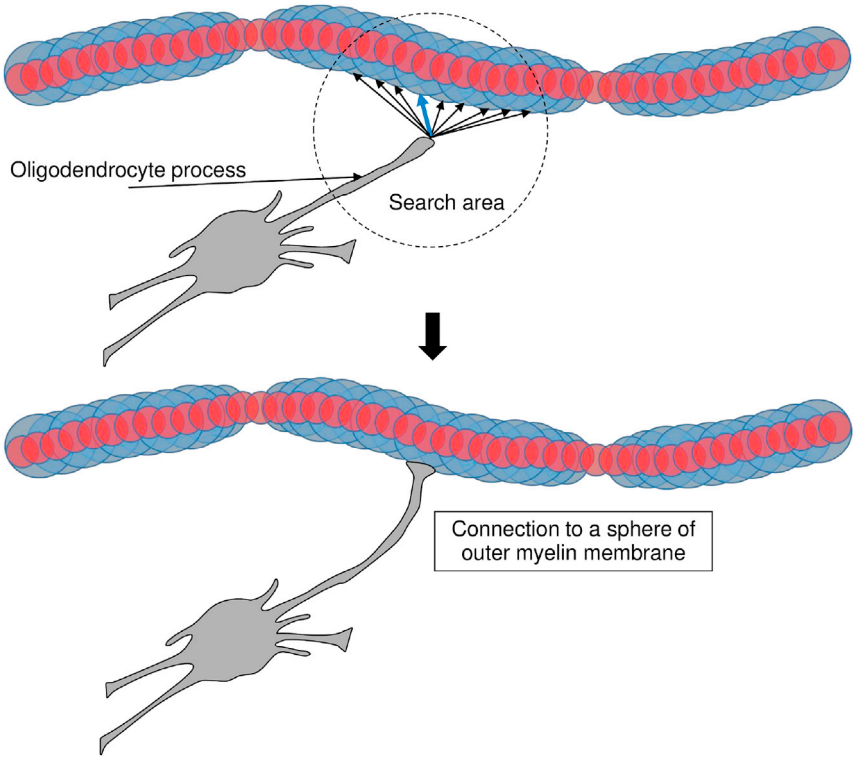

Fig. 6. Illustration of the oligodendrocyte creation procedure. Each oligodendrocyte searches candidate outer axonal membrane spheres within a search area, and connects to one of these. The connection algorithm employs a look-up table to make the search procedure efficient.

necessary displacement to make them non-penetrating.

Let $\mathbf{s}_1 = (x_1, r_1, p_1, c_1)$ and $\mathbf{s}_2 = (x_2, r_2, p_2, c_2)$ be two spheres with centers in position x_i, radius r_i, cell population ID p_i and cell item ID c_i. Two spheres having distinct cell population ID do not belong to the same cell population (one can belong to an astrocyte population, the other to an axonal fiber population for instance), while two spheres having the same cell population ID but distinct cell item ID belong to the same cell population (both belong to the same axonal fiber population for instance) but not to the same element within that population (not the same axonal fiber for instance). The overlap O between those two spheres is

$$O(\mathbf{s}_1, \mathbf{s}_2) = \max(0, r_1 + r_2 - d(x_1, x_2)) \tag{3}$$

where $d(x_1, x_2)$ denotes the Euclidean distance between the two sphere centers.

The repulsion force on $\mathbf{s}_1$ works in the opposite direction to $\mathbf{s}_2$, with a strength linearly dependent on the overlap

$$F(\mathbf{s}_1, \mathbf{s}_2) = \frac{O(\mathbf{s}_1, \mathbf{s}_2)}{2} \frac{x_1 - x_2}{|x_1 - x_2|} \tag{4}$$

For each sphere of the scene, the repulsion force is computed with all other spheres that do not belong to the same item, and the total repulsion force for a sphere $\mathbf{s}_1$ is cumulated over all spheres from distinct items, whose set is denoted by S:

$$F_{tot}(\mathbf{s}_1) = \sum_{\mathbf{s} \in S} F(\mathbf{s}_1, \mathbf{s}) \tag{5}$$

The algorithm is optimized using a 1D sweep and prune algorithm (Avril et al., 2010) that reduces the number of collision checks by sorting the spheres in the voxel using their position projected along an arbitrary axis. This sorting-based algorithm enables an additional ten-fold speed-up.

2.2.2. Stopping criterion and regularization

In order to determine when the collision solver should be stopped, a stopping criterion must be defined. During the packing process, the repulsion forces decrease very fast at the beginning and converge slowly to zero at the end (see Fig. 7).

As emphasized in (Altendorf and Jeulin, 2011), the process should be stopped by a criterion which is dependent on the repulsion forces strength. The total repulsion forces strength is computed at each step as the sum of the norms of each applied repulsion force. The algorithm terminates with a packing solution if the total force strength falls below a certain limit $\alpha s.n$, where s is the size of the bounding box, n is the number of items in the scene and α is an overlap tolerance provided by the user, typically equal to 0.002.

Of course, if the packing density is too high, it is possible that the collision solver may not converge due to the absence of solution to the packing problem. This case is managed with an additional stop criterion based on the maximal number of steps. This maximal number of steps depends on the complexity of the packing problem, but was typically in the range of $50 - 200$ iterations for the here shown examples.

At each step of the collision solving algorithm, once the repulsion forces between all spheres have been applied for this given step, a regularization procedure is performed for the spheres belonging to a given item. The regularization consists in smoothing the deformed items by computing a weighted sum between each sphere position and the mean position of the neighboring spheres within the item. The degree of smoothing is controlled by the number of neighbor positions taken into account, as well as the sum weights. It is important to note that the stronger the smoothing, the slower the convergence rate of the collision solver algorithm.

2.2.3. The particular case of glial cells

Applying repulsion forces on glial cells at each step of the packing algorithm leads to problems related to the conservation of the branching structure, especially for astrocytes. The regularization approach presented in the previous section is sufficient for axonal fibers, but additional constraints have to be added to preserve the shape of each generated glial cell during the packing process. This particular problem is addressed by identifying nodal spheres in each glial cell item, which correspond to spheres belonging to two or more branches of a given process, or directly related to the soma of the cell (see Fig. 10).

Nodal spheres are given an additional label, and all the spheres belonging to a branch of the process between two nodal spheres are given the label of their two nodal spheres. Thus, at each step of the packing process, after the application of repulsion forces on spheres of the glial cell processes, the position of all spheres between two nodal spheres are regularized following the approach of the previous section, so that each branch of a given process is attached to its nodal spheres on both sides. It is important to note that for each process of a given glial cell, the sphere directly related to the soma of the cell is not moved during the packing process. The sphere representing the soma is not moved either, since the algorithm takes care of avoiding the overlap between two soma spheres when creating the initial geometry before the collision solving procedure.

This straightforward regularization approach is only valid if the amplitude of the repulsion forces applied at each step of the algorithm are small enough not to irreversibly degrade the branching structure of the

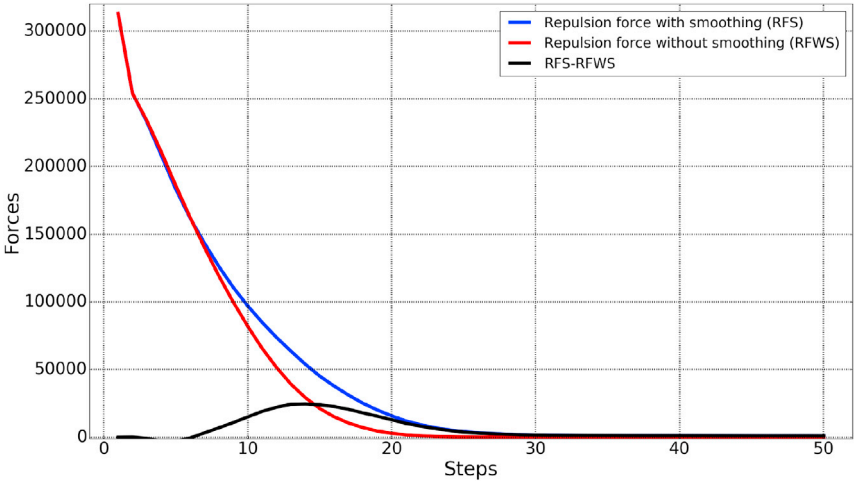

Fig. 7. Evolution of the total repulsion forces (a.u.) during the packing process for an example configuration with a single axonal fiber population with mean diameter $2.0\mu m$ and volume fraction 0.7, with and without the regularization procedure.

cell. This is ensured by bounding the amplitude of each repulsion force to the diameter of the sphere it is applied to.

2.2.4. Data and code availability statement

The data and code that support the results of this study are available from the corresponding author upon request.

3. Results

3.1. Fibers, astrocytes and oligodendrocytes

3.1.1. Fibers

Fig. 8 shows results of the MEDUSA framework to create white matter phantoms composed of one, two or three populations of fibers, with the same geometrical properties for each population, and for 3 fiber volume fractions set to 0.1, 0.4 and 0.7 respectively. In Fig. 9, the degree of geometrical complexity of a phantom with a single fiber population is gradually increased by the successive addition of tortuosity (LAD, see Table 1), global angular dispersion (GAD) and beading. Myelin and Ranvier nodes are also represented in all configurations.

3.1.2. Astrocytes and oligodendrocytes

Fig. 10 illustrates the creation of astrocytes for different values of the balancing factor BF_a controlling the amount of branching. Being able to control the amount of branching is essential to model astrocytes properly. Indeed, it has been reported that astrocyte activation due to CNS pathologies can increase the amount of branching (Pekny and Nilsson, 2005). Fig. 11 shows a realistic example of astrocytes inside a fiber packing and Fig. 12 shows a realistic example of generated oligodendrocytes, which enables to see the connections of the oligodendrocytes with the neighboring axons.

3.2. Examples of generated virtual tissues

As shown previously, the MEDUSA framework enables the creation of distinct cell types in a given virtual tissue. Fig. 13 shows an example of a typical virtual tissue representing a white matter voxel comprising axonal fibers, astrocytes and oligodendrocytes using realistic geometrical parameters. This figure illustrates the capability of MEDUSA to create biomimicking scenes with a high degree of realism very efficiently, without any collision between the different items: a runtime of 56*s* on an NVIDIA DGX1 station was observed, for a realistic voxel size of $100\mu m^3$ as recommended in (Hall et al., 2017) and a total number of spheres inside the voxel of 625000. A reduced number of 32 input parameters was sufficient to generate this virtual tissue and control the geometrical properties of interest for each cell population.

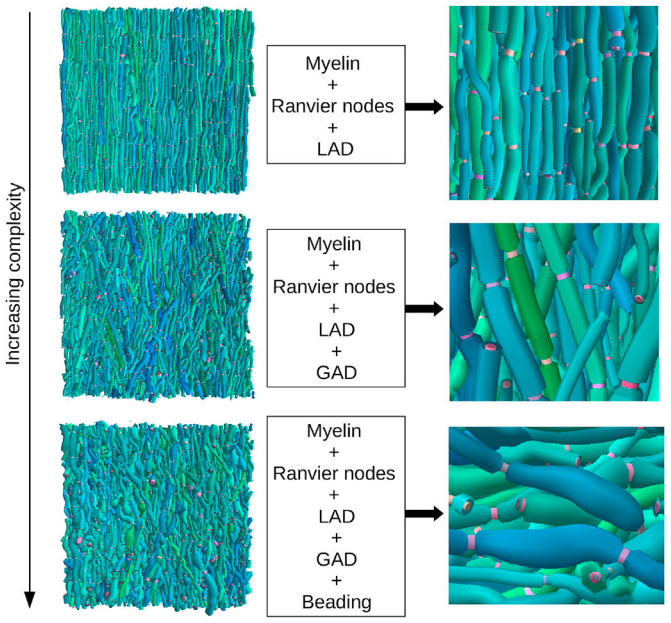

(a) Myelin/ Ranvier nodes / LAD

Fig. 9. Axonal fibers (1 population) generated with the MEDUSA framework with different microstructural details (see Table 1). A mean diameter of $2.0\mu m$ was employed and the voxel size is $100\mu m^3$.

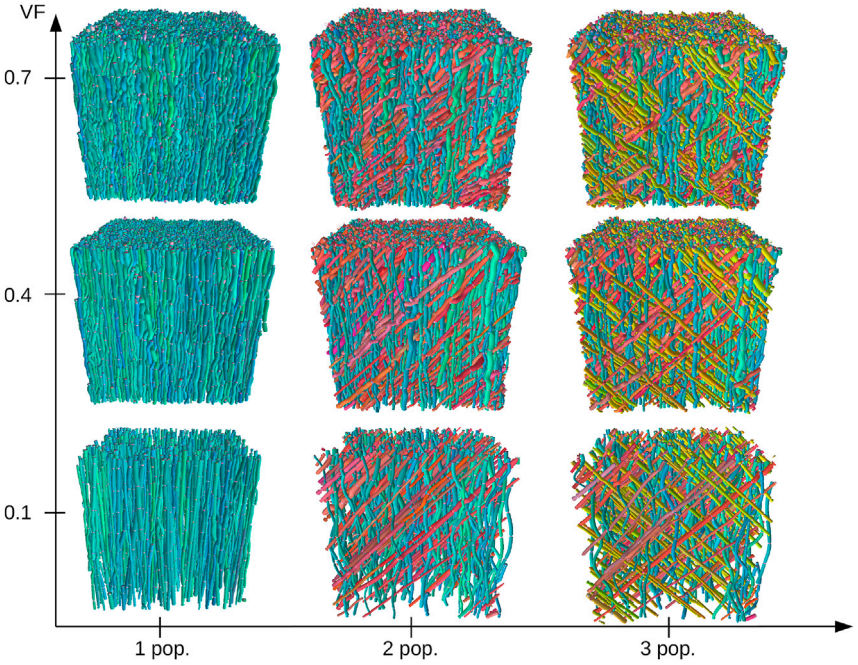

Fig. 8. Example phantoms containing 1, 2 and 3 fiber populations at volume fractions of 0.1, 0.4 and 0.7. A mean diameter of $2.0\mu m$ was employed for each population. The voxel size is $100\mu m^3$.

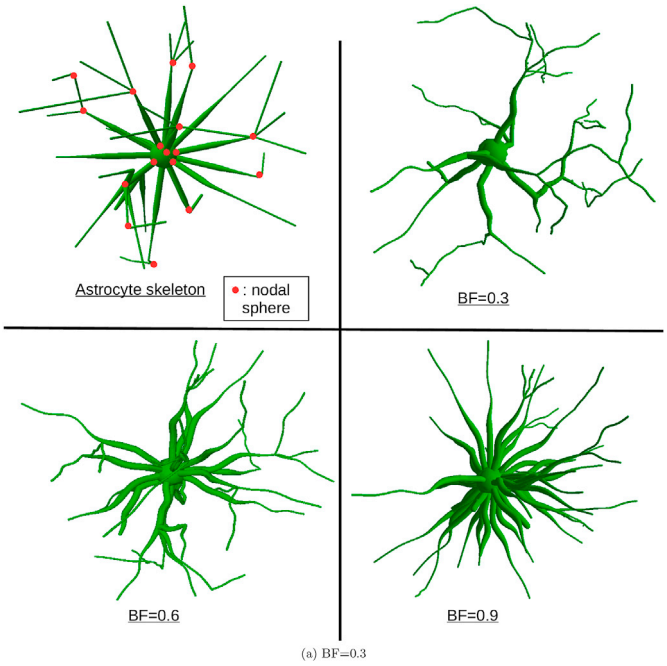

Fig. 10. Astrocytes generated with the MEDUSA framework at 3 values of the balancing factor (BF) are shown. An example astrocyte skeleton (before the application of tortuosity to the processes) illustrating the concept of nodal spheres is also shown. Each branch of an astrocyte process corresponds to a green segment between two nodal spheres.

3.3. Convergence of the MEDUSA framework

Fig. 4 shows the evolution of the repulsion forces during the packing process, for an example configuration with a single axonal fiber population, with and without the regularization procedure, and illustrates the impact of the smoothing procedure on the convergence rate of the packing. The regularization has a reasonable impact on the convergence and is essential to preserve the shapes of the items while applying repulsion forces.

3.4. Packing densities limits

Fig. 14 shows the maximal values of packing densities as a function of global angular dispersion, for one (a.), two (b.) and three (c.) fiber populations which have the same geometrical parameters.

Let n be the amount of fibers and s the size of the bounding box, the packing procedure is considered successful if the remaining repulsion force at the end of runtime falls below $0.002s.n$ after 100 iterations, meaning that the mean sum of necessary displacement in a fiber or cell process is smaller than 0.2 percent of a unit size (Altendorf and Jeulin, 2011).

3.5. Computational efficiency

One important aspect of MEDUSA is that it can be run efficiently on any GPU-capable computer. Fig. 15 shows the computation time in log scale as a function of both the number of spheres inside the scene and the volume fraction. The measures were made using a C++/CUDA implementation of MEDUSA run on a Nvidia DGX1 station. An approximate linear dependence is observed for both cases, illustrating the fact that the computation time grows exponentially with the volume fraction and the number of spheres inside the generated scene.

3.6. Constructing biophysically plausible packings

The well-known Gamma distributions are employed throughout this work to model axonal diameter distributions, and a large value of mean axonal diameter of $2.0\mu m$ is deliberately used to improve the visibility of the constructed fibers in a typical voxel of $100\mu m^3$ in the presented figures, for illustration purposes. However, it is known that Gamma distributions fail to accurately describe the main characteristics of the axon diameter distribution (Sepehrband et al., 2016), and the peak of axonal diameter distributions in the human brain is located below $1.0\mu m$ (Caminiti et al., 2009). Moreover, the standard Watson distributions are employed to model the global angular dispersion of axons. The Watson distribution is used for the sake of simplicity, but assumes an axially symmetric distribution of axons which is not realistic even in the corpus callosum (Schilling et al., 2018).

Nevertheless, MEDUSA is a modular framework, and the choice of these distributions is interchangeable with other more realistic distributions to model white matter axon configurations. It has been found in (Sepehrband et al., 2016) that the *generalized extreme value distribution*, which has one additional unknown parameter with respect to the Gamma distribution, consistently fitted the measured distribution of axonal diameters from white matter electron microscopy images better than other distribution functions. It was also shown that, while having the same number of unknown parameters, the lognormal and inverse Gaussian distributions outperformed the Gamma distribution. Fig. 16 a shows numerical phantoms with mean axonal diameter of $0.4\mu m$ generated with MEDUSA using these various distributions, illustrating the versatility of MEDUSA regarding the choice of an axonal diameter distribution.

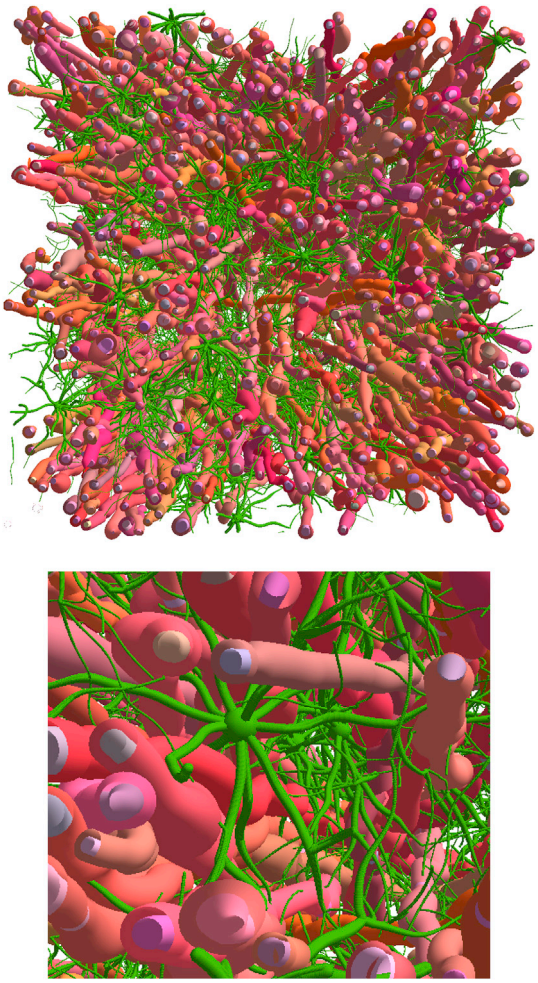

Fig. 11. Realistic scene generated with the MEDUSA framework with astrocytes and fibers. For illustration purposes, a small volume fraction of 0.3 was employed and 200 astrocytes were generated. A mean diameter of $2.0\mu m$ was used for axonal fibers, and the voxel size is $100\mu m^3$.

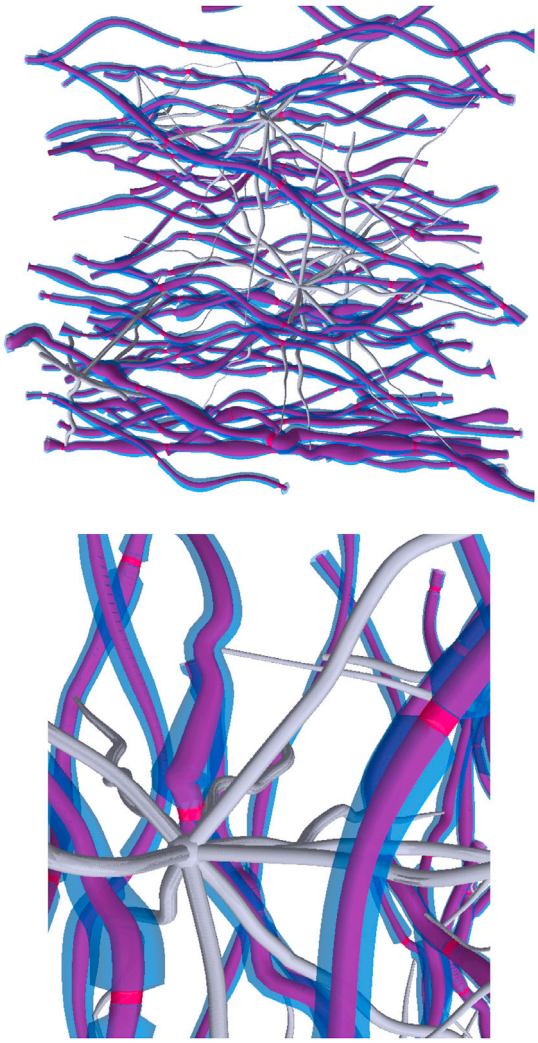

Fig. 12. Realistic scene generated with the MEDUSA framework with oligodendrocytes and fibers. For illustration purposes, a small volume fraction of 0.05 was employed and 5 astrocytes were generated. A mean diameter of 2.0μm was used for axonal fibers, and the voxel size is 100μm^3.

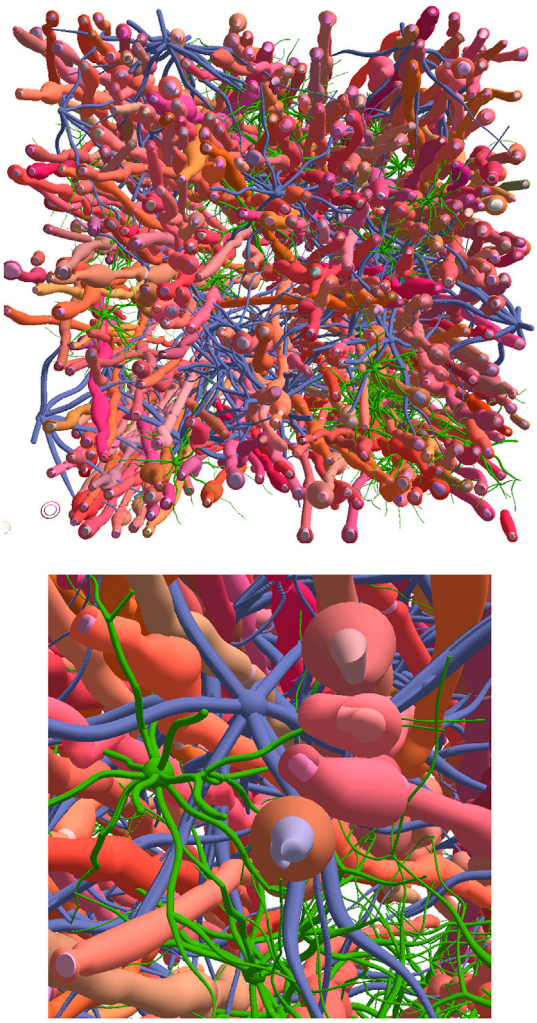

Fig. 13. Realistic scene generated with the MEDUSA framework with astrocytes (in green), oligodendrocytes (in purple) and fibers. For illustration purposes, a small volume fraction of 0.3 was employed and 200 astrocytes and oligodendrocytes were generated. A mean diameter of 2.0μm was used for axonal fibers, and the voxel size is 100μm^3.

In the same vein, the existence of complex fibre configurations, such as fanning and bending axons, gives rise to anisotropic orientation dispersion. Fanning and bending fibres have been shown to be widespread in brain histology data (Türe et al., 2000; Kleinnijenhuis et al., 2013; Budde and Annese, 2013) and diffusion MRI data (Lazar et al., 2005; Sotiropoulos et al., 2012). It is thus essential for MEDUSA to be able to draw axon orientations from a distribution enabling the characterisation of anisotropic orientation dispersion.

The well-known Bingham distribution (Bingham, 1974) has been used in previous work to model and quantify anisotropic orientation dispersion (Tariq et al., 2016). However, the MEDUSA framework requires to draw the orientation of each fiber from the chosen angular dispersion distribution. Obtaining random samples from the Bingham distribution and, more generally, from distributions of the Fisher-Bingham family, requires the use of acceptance-rejection methods (Kent et al., 2013), which can be computationally expensive (Paine et al., 2018) and difficult to implement. An alternative to the Bingham distribution is the angular central Gaussian distribution, which has the additional advantages of being simple and fast to simulate from (Tyler, 1987; Paine et al., 2018; Mardia and Jupp, 2009).

In particular, the elliptically symmetric angular Gaussian distribution (ESAG) (Paine et al., 2018) is well suited to MEDUSA needs, since it enables a simple modeling of anisotropic orientation dispersion of each generated axonal population, is very fast to simulate from, and uses only five parameters. The first three parameters correspond to the vector μ. The mean direction of the axon population is given by $\mu/||\mu||$ and the norm of μ is a measure of the orientation dispersion around this direction.

Due to its ellipse-like constant density contours inscribed on the unit sphere, the ESAG distribution has reflective symmetry about the center of the sphere along two axes orthogonal to each other and to its mean direction. The anisotropy along each of these two axes is quantified by the vector γ, thus enabling a straightforward control of the distribution shape. Fig. 16.b shows numerical phantoms constructed using the ESAG distribution with different levels of dispersion and directional anisotropy, illustrating the ability of MEDUSA to model anisotropic orientation dispersion of axons in an efficient and user-friendly way.

4. Discussion

The MEDUSA framework provides a new way to generate realistic numerical phantoms of the brain white matter. One important property of the MEDUSA paradigm, which consists in decomposing each cell type into a set of overlapping spheres and applying repulsion forces between those spheres, is that the overall structure of the cells is preserved after the application of those forces, thus enabling the creation of highly

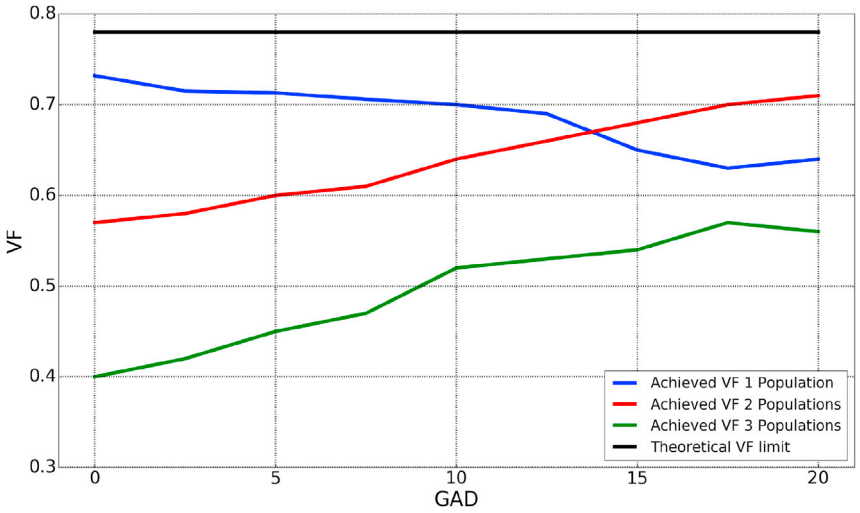

Fig. 14. Maximum achieved volume fraction (or packing density) as a function of the global angular dispersion, for 1, 2 and 3 fiber populations with the same geometrical properties. The theoretical limit corresponds to the case of random packing of 2D discs (Altendorf and Jeulin, 2011).

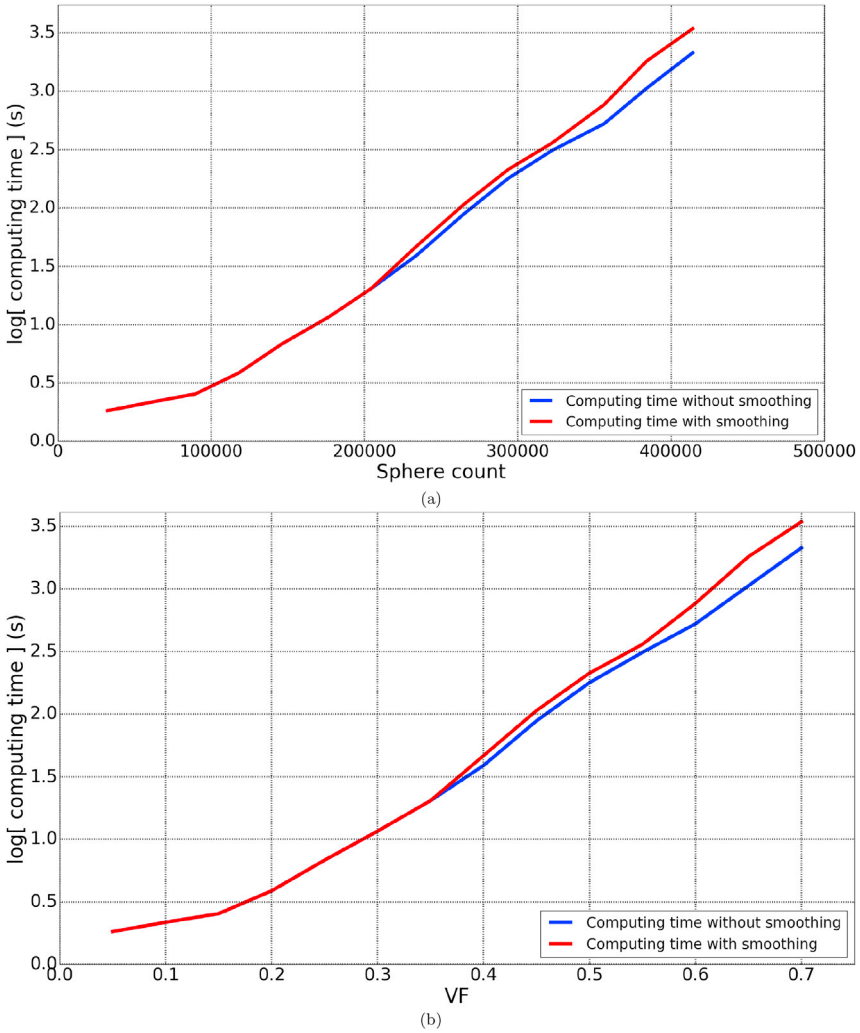

Fig. 15. Computation time of an example packing containing fibers, astrocytes and oligodendrocytes (volume fraction of 0.65) in seconds, as a function of the number of spheres (a) and the achieved volume fraction (b), with or without using the smoothing of objects between each application of the repulsion forces.

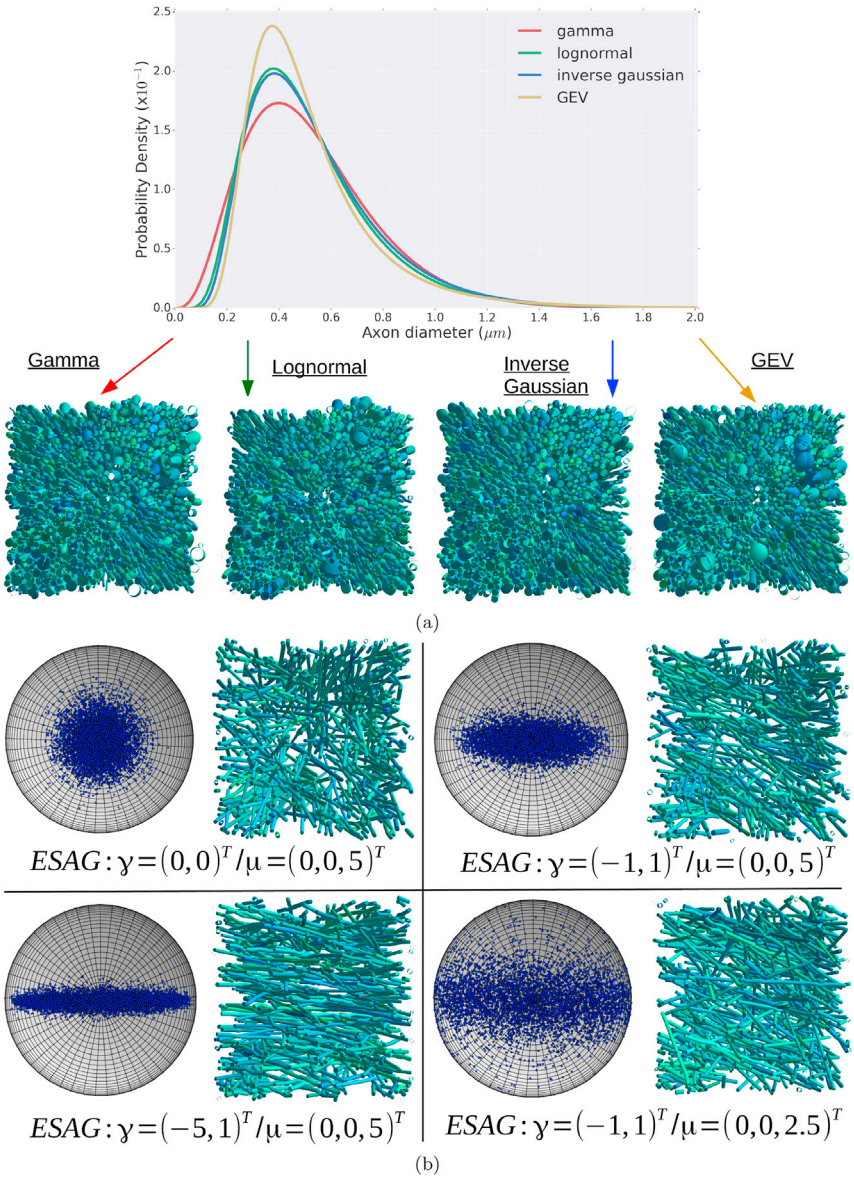

Fig. 16. a. Example MEDUSA phantoms with mean axonal diameter of 0.4μm, packing density of 0.5, using various axonal diameter distributions in a voxel of 20μm^3. **b.** MEDUSA phantoms at various levels of orientation dispersion anisotropy, constructed using the elliptically symmetric angular gaussian distribution (ESAG) to draw axon orientations. The mean direction of the axon population is given by $\mu/||\mu||$ and the norm of μ is a measure of the orientation dispersion around this direction. The anisotropy along each of the symmetry axes is quantified by the vector γ, thus enabling a straightforward control of the distribution shape.

realistic scenes without any collision. As illustrated in Fig. 13, the spherical decomposition technique enables to create all types of cells with a high degree of realism which is equivalent to triangular mesh approaches.

4.1. MEDUSA: a novel generative framework

4.1.1. Controlling cell morphologies

MEDUSA represents a novel tool to perform ground-truth controlled studies of brain white matter tissues and thus better understand the particular effect of different geometrical properties of the white matter tissues (beading of axons, presence of astrocytes and oligodendrocytes) on the observed diffusion MRI signal using Monte-Carlo simulations of the diffusion process (Hall and Alexander, 2009; Yeh et al., 2013). The synthesis of diffusion MRI signals from the generated geometries can also be used to assess the validity of white matter multicompartment models (Zhang et al., 2012; Jespersen et al., 2007; Dyrby et al., 2013; Alexander et al., 2010; Assaf and Basser, 2005; Assaf et al., 2008) and the robustness of their parameter estimation when introducing finer degrees of structural complexity in the phantoms, such as the tortuosity of axons, which is not accounted for in current analytical models.

The fact that the MEDUSA framework enables the fast creation of a realistic tissue, with a reduced set of parameters giving a full control over the geometrical properties of the generated tissue, paves the way to the construction of a dictionary of white matter geometrical configurations. Such a dictionary would include millions of geometries representing all possible white matter geometrical configurations over a wide range of realistic parameter values. Computing the diffusion MRI signal associated to each of these geometries using Monte-Carlo simulations would enable to use machine learning techniques to model the relationship between the measured diffusion MRI signal and the underlying tissue properties, thus creating a DW-NMR signature of corresponding microstructural features.

While the efficiency of such an approach is still putative, being able to fastly generate realistic numerical phantoms of white matter and their associated diffusion-weighted signals will at least prove useful to optimize diffusion-weighting sequence parameters, in order to increase sensitivity to certain biophysical properties of interest, such as axon diameter or myelin thickness.

4.1.2. High packing densities

In the presence of global angular dispersion and multiple fiber

populations, the MEDUSA framework enables to reach much higher values of fiber packing densities than previous frameworks such as the latest version of DMS (Ginsburger et al., 2018). We observe in Fig. 14 that in the case of a single fiber population, small values of global angular dispersion (GAD) enable to reach a high volume fraction of approximately 0.72. This low value of angular dispersion is equivalent to the z-axis preferred orientation distribution which yielded the highest volume fraction in (Altendorf and Jeulin, 2011).

Still in the case of a single fiber population, an increasing GAD yields to a diminution of the highest achieved volume fraction, which is consistent with observations in (Altendorf and Jeulin, 2011) and is due to the fact that increasing GAD shifts the packing procedure from a random packing of 2D discs when $GAD = 0$ degree, for which the maximal volume fraction can reach up to 0.78 (Altendorf and Jeulin, 2011), to a general 3D packing problem.

On the contrary, a positive effect of increasing GAD is observed in Fig. 14 on the highest achieved volume fraction in the case of multiple fiber populations, due to the fact that the introduction of GAD diminishes the discrepancy between the direction of the fibers of different populations.

However, while the two populations case still enables to reach high volume fractions up to 0.71, the highest achieved volume fraction with three populations goes down to 0.57. This is still a huge improvement with respect to previous approaches (Ginsburger et al., 2018).

4.1.3. Convergence

As explained before, the packing algorithm terminates with a valid solution if the total repulsion force strength falls below a certain limit αn, where n is the number of items in the scene and α is an overlap tolerance provided by the user. This convergence rule is somehow arbitrary and, by definition, does not guarantee the absence of overlap if a non null tolerance value is provided. To ensure a non-overlapping system, a final step could be added, as mentioned in (Altendorf and Jeulin, 2011), where the radius of each sphere is reduced according to the maximal overlap with other spheres. In this case however, the axon radius does not remain constant along the fiber centroid.

4.2. Outlook

4.2.1. Creating dictionaries of virtual tissues and their DW-NMR signatures

The MEDUSA framework is particularly adapted to the creation of a dictionary of synthetic white matter geometries, due to several advantages:

- its ability to reach high values of packing density even at high values of global angular dispersion of the axonal fibers
- the modeling of advanced properties of axonal fibers such as tortuosity, beading, myelin sheath and Ranvier nodes, and the ability to represent various type of white matter cells (astrocytes and oligodendrocytes)
- the low computation time for each phantom (see Fig. 15 for typical computing times on a Nvidia DGX1 station)

In the prospect of creating a dictionary of synthesized diffusion MRI signals associated to each generated geometry, the sphere decomposition is also very convenient. Indeed, when performing Monte-Carlo simulations of the diffusion process in the generated phantoms, the decomposition of objects into spheres enables a diminution of the computational time (measured up to 70%), due to the fact that the collision checking between diffusing particles (spins) and the cell membranes is more efficient with spheres than with a triangular mesh. Provided that a one-to-one mapping exists between each generated substrate and the corresponding synthesized signal in the diffusion MRI space, which notably depends on the employed diffusion-weighting MRI sequence, such a dictionary-based machine learning approach could prove useful to inversely decode white matter microstructure. While remaining very challenging, such an approach is one of the main motivations and potential outlooks of the MEDUSA framework.

4.2.2. 3D-PLI as a use case beyond diffusion MRI

Due to their high degree of realism, the virtual tissues generated with MEDUSA could also be used to simulate light microscopic measurements, such as 3D Polarized Light Imaging (3D-PLI) (Axer et al., 2011a, b; Larsen et al., 2007; Zilles et al., 2016). 3D-PLI is a technique for analyzing the fiber architecture of myelinated axons in unstained histological brain sections at the micrometer level. The regularly arranged lipids in the myelin sheaths induce optical birefringence, which allows to extract the local orientation of myelinated axons similar to diffusion MRI but at much higher resolution.

Simulations of 3D-PLI measurements (Dohmen et al., 2015; Menzel et al., 2015b) require tissue phantoms that define the local optical properties, i.e. the local optic axis (Dohmen et al., 2015; Menzel et al., 2015b) or refractive indices (Dohmen et al., 2015; Menzel et al., 2015a) which can easily be assigned to the different neuronal components (e.g. axon, myelin, extracellular space) generated by MEDUSA. Using the same virtual tissues with different imaging techniques, such as diffusion MRI and 3D-PLI, could enable to better understand the relationship and complementarity between images obtained from these two modalities. This latter aspect will be addressed in future studies.

4.2.3. Towards gray matter virtual tissues

The MEDUSA framework was here presented as a tool to create realistic phantoms of the brain white matter. However, the generic approach shown here, relying on the sphere decomposition and the application of repulsion forces to avoid collision between objects, can be adapted to construct gray matter phantoms.

The construction of a wide variety of different neural cell types, as was done in (Cuntz et al., 2010; Palombo et al., 2018), is out of the scope of this work. However, in order to illustrate the ability of the MEDUSA framework to adapt to gray matter, an example phantom comprising simple stellate cells at a packing density of 0.32 is shown in Fig. 17. The employed algorithm to generate such cells is similar to the one used to construct astrocytes, based on the computation of a minimum spanning tree as explained earlier.

The adaptation of MEDUSA to more complex neural cell shapes, such as Purkinje or pyramidal cells, only necessitates to modify the algorithm creating the node points from which the minimum spanning tree is computed, using for instance a preliminar tree generation algorithm as described in (Palombo et al., 2018). The ability of MEDUSA to generate

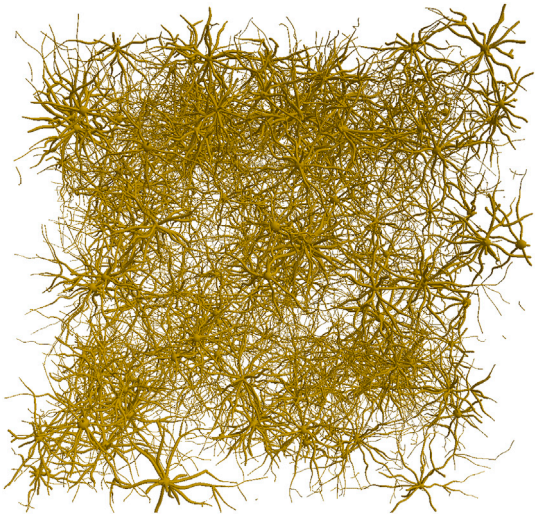

Fig. 17. Example phantom containing stellate neural cells at a volume fraction of 0.32, showing the potential application of the MEDUSA framework to gray matter phantom generation.

astrocytes with controlled geometrical properties could also be used to model activated gray matter astrocytes (due to plasticity for instance) whose shapes are modified during activation, with an observed increase in the number of processes and in their perimeter and volume (Theodosis et al., 2008; Blumenfeld-Katzir et al., 2011).

4.3. Limitations and future work

4.3.1. Biophysical realism

The high representational power of MEDUSA enables to construct a large variety of cell shapes while ensuring the absence of collision in a given voxel, thus fulfilling all the essential requirements to obtain realistic white matter substrates. However, the actual realism of the substrates still depends on the exactness of the assumptions used for the characterisation of the generated white matter tissues. To this end, the ongoing field of research of 3D axonal morphometry (Xu et al., 2018; Lee et al., 2018; Abdollahzadeh et al., 2017) is essential to improve our knowledge of the axonal shape and the fiber orientation dispersion. In particular, the assumption of circular axonal cross-sections used in this paper might not stand, as suggested in (Xu et al., 2018; Abdollahzadeh et al., 2017; Lee et al., 2018), where elliptical cross-sections have been considered more plausible. Similarly, the use of elliptically symmetric angular Gaussian distributions proposed in this work to improve the realism of axonal orientation dispersion modeling with respect to Watson distributions has to be carefully validated with the help of 3-dimensional histology.

4.3.2. Boundary conditions

MEDUSA generates 3-dimensional packings with geometrical discontinuities over the boundaries, which could introduce an additional restricted diffusion effect corresponding to the box size when using a periodic boundary condition as in (Hall and Alexander, 2009). We thus recommend to employ a mirroring (or reflective) boundary condition at the bounding box when performing Monte-Carlo simulations using MEDUSA phantoms. However, while preventing microstructural discontinuity over the boundary (Fieremans et al., 2010), mirroring may result in increased fiber orientation dispersion, which needs to be quantified in future work.

4.3.3. Vascular compartment

The presence of vascular compartments in white matter is neglected in the generated substrates. While these vascular compartments are invisible at high *b*-values, they contribute to the IVIM signal at low *b*-values (Fournet et al., 2017; Li et al., 2012). Including such compartments would require an hybrid branching algorithm, similar to the one used for astrocytes creation, and allowing to control the distribution of diameters of generated vessels, arteries and capillaries. Microvascular networks adapted from (Novikov et al., 2018) or (Gagnon et al., 2015) could also be used.

4.3.4. Packing-induced tortuosity

On another front, the fact of using a set of spheres instead of a cylinder to represent a fiber gives a lot more degrees of freedom to solve the packing problem. It is however worth noting that the proposed packing algorithm yields the creation of a certain amount of tortuosity among axonal fibers, induced by the application of repulsion forces. While such a phenomenon is not a problem itself since similar effects can be observed in actual white matter axonal packings (Nilsson et al., 2012), the detrimental effect is that the obtained value of tortuosity for a given fiber population differs from the value required by the user when constructing the virtual scene.

While this effect is quite negligible at small volume fractions, it can significantly alter the obtained value of tortuosity at high volume fractions: for instance, a tortuosity of 12° is induced by the sole application of repulsion forces at a volume fraction of 0.7 for a single fiber population with a global angular dispersion of 10°.

If the tortuosity value required by the user is big enough to "absorb" this induced tortuosity, this effect is corrected for by diminishing the amount of tortuosity induced by applying Gaussian deformations to the fibers. In the event that the actual value of tortuosity differs from the input value required by the user, the amount of tortuosity is computed again at the end of the phantom generation procedure and potential discrepancies are noted by the algorithm.

5. Conclusion

The MEDUSA framework enables the fast generation of realistic phantoms of white matter, comprising different types of cells, while efficiently avoiding collisions thanks to a spherical decomposition of the shapes. The presented approach can be generalized to any type of cells in the white and gray matter, and is an important step in the investigation of the microstructure of brain tissues. Since MEDUSA enables to control the geometrical properties of the generated phantoms, it is indeed an efficient tool to generate a wide variety of configurations, which can be seen as a dictionary of all possible samples of brain tissues in a given voxel. Future work will consist in widening the MEDUSA framework to a larger variety of brain cells, such as specific types of neurons, and creating phantoms of multiple voxels catching the structure and organization of the brain at a mesoscopic scale.

Conflicts of interest

The authors declare that the research was conducted in the absence of any commercial or financial relationships that could be construed as a potential conflict of interest.

Author contributions

KG, FM, JFM, MA and CP designed research. KG and CP wrote the paper. KG, FM, CP and FP developed the MEDUSA software.

Funding

This project has received funding from the European Unions Horizon 2020 Research and Innovation Program under Grant Agreement No. 785907 (HBP SGA2).

References

Abdollahzadeh, A., Belevich, I., Jokitalo, E., Tohka, J., Sierra, A., 2017. 3d axonal morphometry of white matter. bioRxiv. https://doi.org/10.1101/239228.
Alexander, D.C., Hubbard, P.L., Hall, M.G., Moore, E.A., Ptito, M., Parker, G.J., Dyrby, T.B., 2010. Orientationally invariant indices of axon diameter and density from diffusion mri. Neuroimage 52, 1374–1389.
Altendorf, H., Jeulin, D., 2011. Random-walk-based stochastic modeling of three-dimensional fiber systems. Phys. Rev. 83, 041804.
Assaf, Y., Basser, P.J., 2005. Composite hindered and restricted model of diffusion (charmed) mr imaging of the human brain. Neuroimage 27, 48–58.
Assaf, Y., Blumenfeld-Katzir, T., Yovel, Y., Basser, P.J., 2008. Axcaliber: a method for measuring axon diameter distribution from diffusion mri. Magn. Reson. Med. 59, 1347–1354.
Avril, Q., Gouranton, V., Arnaldi, B., 2010. A broad phase collision detection algorithm adapted to multi-cores architectures. In: Vric 2010 Proceedings, p. 95.
Axer, M., Amunts, K., Grässel, D., Palm, C., Dammers, J., Axer, H., Pietrzyk, U., Zilles, K., 2011a. A novel approach to the human connectome: ultra-high resolution mapping of fiber tracts in the brain. Neuroimage 54, 1091–1101.
Axer, M., Grässel, D., Kleiner, M., Dammers, J., Dickscheid, T., Reckfort, J., Hütz, T., Eiben, B., Pietrzyk, U., Zilles, K., et al., 2011b. High-resolution fiber tract reconstruction in the human brain by means of three-dimensional polarized light imaging. Front. Neuroinf. 5, 34.
Balls, G.T., Frank, L.R., 2009. A simulation environment for diffusion weighted mr experiments in complex media. Magn. Reson. Med. Official J. Int. Soc. Magn. Reson. Med. 62, 771–778.
Beaulieu, C., 2002. The basis of anisotropic water diffusion in the nervous system a technical review. NMR Biomed. 435–455.
Behrens, T.E., Berg, H.J., Jbabdi, S., Rushworth, M.F., Woolrich, M.W., 2007. Probabilistic diffusion tractography with multiple fibre orientations: what can we gain? Neuroimage 34, 144–155.
Bingham, C., 1974. An antipodally symmetric distribution on the sphere. Ann. Stat. 1201–1225.
Blumenfeld-Katzir, T., Pasternak, O., Dagan, M., Assaf, Y., 2011. Diffusion mri of structural brain plasticity induced by a learning and memory task. PLoS One 6, e20678.

Budde, M.D., Annese, J., 2013. Quantification of anisotropy and fiber orientation in human brain histological sections. Front. Integr. Neurosci. 7, 3.
Budde, M.D., Frank, J.A., 2010. Neurite beading is sufficient to decrease the apparent diffusion coefficient after ischemic stroke. Proc. Natl. Acad. Sci. Unit. States Am. 107, 14472–14477.
Caminiti, R., Ghaziri, H., Galuske, R., Hof, P.R., Innocenti, G.M., 2009. Evolution amplified processing with temporally dispersed slow neuronal connectivity in primates. Proc. Natl. Acad. Sci. Unit. States Am. 106 (46), 19551–19556.
Cuntz, H., Forstner, F., Borst, A., Häusser, M., 2010. One rule to grow them all: a general theory of neuronal branching and its practical application. PLoS Comput. Biol. 6, e1000877.
Daducci, A., Dal Palú, A., Descoteaux, M., Thiran, J.P., 2016. Microstructure informed tractography: pitfalls and open challenges. Front. Neurosci. 10.
del Río-Hortega, P., 1928. Tercera aportacion al conocimiento morfologico e interpretacion funcional de la oligodendroglia.
Dohmen, M., Menzel, M., Wiese, H., Reckfort, J., Hanke, F., Pietrzyk, U., Zilles, K., Amunts, K., Axer, M., 2015. Understanding fiber mixture by simulation in 3d polarized light imaging. Neuroimage 111, 464–475.
Dyrby, T.B., Hall, M.G., Ptito, M., Alexander, D., et al., 2013. Contrast and stability of the axon diameter index from microstructure imaging with diffusion mri. Magn. Reson. Med. 70, 711–721.
Fieremans, E., Novikov, D.S., Jensen, J.H., Helpern, J.A., 2010. Monte Carlo study of a two-compartment exchange model of diffusion. NMR Biomed. 23, 711–724.
Fisher, N.I., Lewis, T., Embleton, B.J., 1993. Statistical Analysis of Spherical Data. Cambridge university press.
Fournet, G., Li, J.R., Cerjanic, A.M., Sutton, B.P., Ciobanu, L., Le Bihan, D., 2017. A two-pool model to describe the ivim cerebral perfusion. J. Cereb. Blood Flow Metab. 37, 2987–3000.
Gagnon, L., Sakadžić, S., Lesage, F., Musacchia, J.J., Lefebvre, J., Fang, Q., Yücel, M.A., Evans, K.C., Mandeville, E.T., Cohen-Adad, J., et al., 2015. Quantifying the microvascular origin of bold-fmri from first principles with two-photon microscopy and an oxygen-sensitive nanoprobe. J. Neurosci. 35, 3663–3675.
Ginsburger, K., Poupon, F., Beaujoin, J., Estournet, D., Matuschke, F., Mangin, J.F., Axer, M., Poupon, C., 2018. Improving the realism of white matter numerical phantoms: a step toward a better understanding of the influence of structural disorders in diffusion mri. Frontiers in Physics 6, 12.
Hall, M.G., Alexander, D.C., 2009. Convergence and parameter choice for monte-carlo simulations of diffusion mri. IEEE Trans. Med. Imaging 28, 1354–1364.
Hall, M.G., Nedjati-Gilani, G., Alexander, D.C., 2017. Realistic Voxel Sizes and Reduced Signal Variation in Monte-Carlo Simulation for Diffusion Mr Data Synthesis. 1701.03634.
Harkins, K.D., Does, M.D., 2016. Simulations on the influence of myelin water in diffusion-weighted imaging. Phys. Med. Biol. 61, 4729.
Jespersen, S.N., Kroenke, C.D., Østergaard, L., Ackerman, J.J., Yablonskiy, D.A., 2007. Modeling dendrite density from magnetic resonance diffusion measurements. Neuroimage 34, 1473–1486.
Kent, J.T., Ganeiber, A.M., Mardia, K.V., 2013. A New Method to Simulate the Bingham and Related Distributions in Directional Data Analysis with Applications. 1310.8110.
Kleinnijenhuis, M., Zhang, H., Wiedermann, D., Kusters, B., Norris, D., van Cappellen van Walsum, A., 2013. Detailed laminar characteristics of the human neocortex revealed by noddi and histology. In: Proc. 19th Annual Meeting of the OHBM, OHBM, WA, USA (2013), p. 3815.
Landman, B.A., Farrell, J.A., Smith, S.A., Reich, D.S., Calabresi, P.A., van Zijl, P.C., 2010. Complex geometric models of diffusion and relaxation in healthy and damaged white matter. NMR Biomed. An Int. J. Devoted to the Dev. Appl. Magn. Reson. In vivo 23, 152–162.
Larsen, L., Griffin, L.D., GRäßel, D., Witte, O.W., Axer, H., 2007. Polarized light imaging of white matter architecture. Microsc. Res. Tech. 70, 851–863.
Lazar, M., Lee, J.H., Alexander, A.L., 2005. Axial asymmetry of water diffusion in brain white matter. Magn. Reson. Med. An Official J. Int. Soci. Magn. Reson. Med. 54, 860–867.
Lee, H.H., Yaros, K., Veraart, J., Pathan, J., Liang, F.X., Kim, S.G., Novikov, D.S., Fieremans, E., 2018. Electron microscopy 3-dimensional segmentation and quantification of axonal dispersion and diameter distribution in mouse brain corpus callosum. bioRxiv. https://doi.org/10.1101/357491.
Li, J.R., Le Bihan, D., Nguyen, T.Q., Grebenkov, D., Poupon, C., Haddar, H., 2012. Analytical and Numerical Study of the Apparent Diffusion Coefficient in Diffusion Mri at Long Diffusion Times and Low B-Values. Internal Report, INRIA HAL Id: Hal-00763885, 2012.
Lin, M., He, H., Schifitto, G., Zhong, J., 2016. Simulation of changes in diffusion related to different pathologies at cellular level after traumatic brain injury. Magn. Reson. Med. 76, 290–300.
Liu, C., Bammer, R., Acar, B., Moseley, M.E., 2004. Characterizing non-Gaussian diffusion by using generalized diffusion tensors. Magn. Reson. Med. An Official J. Int. Soc. Magn. Reson. Med. 51, 924–937.
Lundgaard, I., Osório, M.J., Kress, B., Sanggaard, S., Nedergaard, M., 2014. White matter astrocytes in health and disease. Neuroscience 276, 161–173.
Marco, P., Clemence, L., Edwin, H.G., Julien, V., 2018. Can we detect the effect of spines and leaflets on the diffusion of brain intracellular metabolites? Neuroimage 182, 283–293.
Mardia, K.V., Jupp, P.E., 2009. Directional Statistics. Volume 494. John Wiley & Sons.
Menzel, M., Axer, M., De Raedt, H., Michielsen, K., 2015a. Finite-difference time-domain simulation for three-dimensional polarized light imaging. In: International Workshop on Brain-Inspired Computing. Springer, pp. 73–85.
Menzel, M., Michielsen, K., De Raedt, H., Reckfort, J., Amunts, K., Axer, M., 2015b. A jones matrix formalism for simulating three-dimensional polarized light imaging of brain tissue. J. R. Soc. Interface 12, 20150734.
Mingasson, T., Duval, T., Stikov, N., Cohen-Adad, J., 2017. Axonpacking: an open-source software to simulate arrangements of axons in white matter. Front. Neuroinf. 11, 5.
Nedjati-Gilani, G.L., Schneider, T., Hall, M.G., Cawley, N., Hill, I., Ciccarelli, O., Drobnjak, I., Wheeler-Kingshott, C.A.G., Alexander, D.C., 2017. Machine learning based compartment models with permeability for white matter microstructure imaging. Neuroimage 150, 119–135.
Neher, P.F., Laun, F.B., Stieltjes, B., Maier-Hein, K.H., 2014. Fiberfox: facilitating the creation of realistic white matter software phantoms. Magn. Reson. Med. 72, 1460–1470.
Neuman, C., 1974. Spin echo of spins diffusing in a bounded medium. J. Chem. Phys. 60, 4508–4511.
Nilsson, M., Latt, J., Staahlberg, F., Westen, D., Hagslatt, H., 2012. The importance of axonal undulation in diffusion mr measurements: a Monte Carlo simulation study. NMR Biomed. 25, 795–805.
Novikov, D.S., Reisert, M., Kiselev, V.G., 2018. Effects of mesoscopic susceptibility and transverse relaxation on diffusion nmr. J. Magn. Reson. 293, 134–144.
Oberheim, N.A., Takano, T., Han, X., He, W., Lin, J.H., Wang, F., Xu, Q., Wyatt, J.D., Pilcher, W., Ojemann, J.G., et al., 2009. Uniquely hominid features of adult human astrocytes. J. Neurosci. 29, 3276–3287.
Paine, P., Preston, S.P., Tsagris, M., Wood, A.T., 2018. An elliptically symmetric angular Gaussian distribution. Stat. Comput. 28, 689–697.
Palombo, M., Alexander, D.C., Zhang, H., 2018. A Generative Model of Realistic Brain Cells with Application to Numerical Simulation of Diffusion-Weighted Mr Signal. 1806.07125.
Pekny, M., Nilsson, M., 2005. Astrocyte activation and reactive gliosis. Glia 50, 427–434.
Rensonnet, G., Scherrer, B., Girard, G., Jankovski, A., Warfield, S.K., Macq, B., Thiran, J.P., Taquet, M., 2019. Towards microstructure fingerprinting: estimation of tissue properties from a dictionary of Monte Carlo diffusion mri simulations. Neuroimage 184, 964–980.
Rushton, W., 1951. A theory of the effects of fibre size in medullated nerve. J. Physiol. 101–122.
Salzer, J.L., 1997. Clustering sodium channels at the node of ranvier: close encounters of the axonglia kind. Neuron 843–846.
Schilling, K.G., Janve, V., Gao, Y., Stepniewska, I., Landman, B.A., Anderson, A.W., 2018. Histological validation of diffusion mri fiber orientation distributions and dispersion. Neuroimage 165, 200–221.
Sen, P.N., Basser, P.J., 2005. A model for diffusion in white matter in the brain. Biophys. J. 89, 2927–2938.
Sepehrband, F., Alexander, D.C., Clark, K.A., Kurniawan, N.D., Yang, Z., Reutens, D.C., 2016. Parametric probability distribution functions for axon diameters of corpus callosum. Front. Neuroanat. 10, 59.
Sotiropoulos, S.N., Behrens, T.E., Jbabdi, S., 2012. Ball and rackets: inferring fiber fanning from diffusion-weighted mri. Neuroimage 60, 1412–1425.
Stanisz, G.J., Wright, G.A., Henkelman, R.M., Szafer, A., 1997. An analytical model of restricted diffusion in bovine optic nerve. Magn. Reson. Med. 37, 103–111.
Szafer, A., Zhong, J., Gore, J.C., 1995. Theoretical model for water diffusion in tissues. Magn. Reson. Med. 33, 697–712.
Tang-Schomer, M.D., Johnson, V.E., Baas, P.W., Stewart, W., Smith, D.H., 2012. Partial interruption of axonal transport due to microtubule breakage accounts for the formation of periodic varicosities after traumatic axonal injury. Exp. Neurol. 233, 364–372.
Tariq, M., Schneider, T., Alexander, D.C., Wheeler-Kingshott, C.A.G., Zhang, H., 2016. Bingham–noddi: mapping anisotropic orientation dispersion of neurites using diffusion mri. Neuroimage 133, 207–223.
Theodosis, D.T., Poulain, D.A., Oliet, S.H., 2008. Activity-dependent structural and functional plasticity of astrocyte-neuron interactions. Physiol. Rev. 88, 983–1008.
Türe, U., Yaşargil, M.G., Friedman, A.H., Al-Mefty, O., 2000. Fiber dissection technique: lateral aspect of the brain. Neurosurgery 47, 417–427.
Tyler, D.E., 1987. Statistical analysis for the angular central Gaussian distribution on the sphere. Biometrika 74, 579–589.
Van Nguyen, D., Grebenkov, D., Le Bihan, D., Li, J.R., 2015. Numerical study of a cylinder model of the diffusion mri signal for neuronal dendrite trees. J. Magn. Reson. 252, 103–113.
Van Nguyen, K., Garzon, E.H., Valette, J., 2018. Efficient gpu-based monte-carlo simulation of diffusion in real astrocytes reconstructed from confocal microscopy. J. Magn. Reson. 296, 188–199.
Vangelderen, P., DesPres, D., Vanzijl, P., Moonen, C., 1994. Evaluation of restricted diffusion in cylinders. phosphocreatine in rabbit leg muscle. J. Magn. Reson., Ser. B 103, 255–260.
Xu, T., Foxley, S., Kleinnijenhuis, M., Chen, W.C., Miller, K.L., 2018. The effect of realistic geometries on the susceptibility-weighted mr signal in white matter. Magn. Reson. Med. 79, 489–500.
Yeh, C.H., Schmitt, B., Le Bihan, D., Li-Schlittgen, J.R., Lin, C.P., Poupon, C., 2013. Diffusion microscopist simulator: a general Monte Carlo simulation system for diffusion magnetic resonance imaging. PLoS One 8, e76626.
Zhang, H., Schneider, T., Wheeler-Kingshott, C.A., Alexander, D.C., 2012. Noddi: practical in vivo neurite orientation dispersion and density imaging of the human brain. Neuroimage 61, 1000–1016.
Zilles, K., Palomero-Gallagher, N., Gräßel, D., Schlömer, P., Cremer, M., Woods, R., Amunts, K., Axer, M., 2016. High-resolution fiber and fiber tract imaging using polarized light microscopy in the human, monkey, rat, and mouse brain. In: Axons and Brain Architecture. Elsevier, pp. 369–389.